INTERNATIONAL JOURNAL OF HYDROGEN ENERGY 40 (2015) 14551–14561

Available online at www.sciencedirect.com

ScienceDirect

journal homepage: www.elsevier.com/locate/he

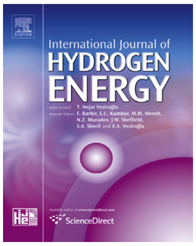

A generic physical model for a thermally integrated high-temperature PEM fuel cell and sodium alanate tank system

Andreas G. Yiotis[*], *Michael E. Kainourgiakis*, *Georgia C. Charalambopoulou*, *Athanassios K. Stubos*

Environmental Research Laboratory, National Center for Scientific Research 'Demokritos', 15310 Athens, Greece

ARTICLE INFO

Article history:
Received 13 March 2015
Received in revised form
28 May 2015
Accepted 29 May 2015
Available online 20 June 2015

Keywords:
H_2 storage tanks
Thermal coupling
Sodium alanate
High temperature PEM fuel cell
Physical model

ABSTRACT

We study the thermal coupling potential between a Sodium Alanate tank and a High-Temperature PEM fuel cell using a heat transfer fluid to redirect a fraction of the thermal power produced during normal fuel cell operation towards the walls of the metal hydride tank in order to maintain hydrogen desorption. The remaining thermal power is then rejected to the environment by introducing an appropriately adjusted excess of air directly to the fuel cell cathode. Assuming a typical tubular geometry for both the metal hydride tank and the fuel cell, we propose a generic physical model that accounts for heat transfer in all the components of the integrated system (fuel cell, metal hydride tank and heating jacket), as well as H_2 desorption kinetics and flow in the tank. Based on this model we study the dynamics of the coupled storage/usage system in terms of H_2 pressure in the tank and temperatures in the tank and the fuel cell. Focus is primarily placed on the parameters that lead to steady-state operating conditions (i.e. the flow rate of air towards the fuel cell and the velocity of the heat transfer fluid in the heating jacket), with respect to the electrical power of the fuel cell.

Introduction

Among the main technological and economic challenges that have to be addressed to enable the widespread use of hydrogen-powered devices and vehicles is the need for combined improvements in both fuel cell (FC) and H_2 storage technologies to bring closer to reality the development of cost-effective, integrated storage and usage systems. The materials-based hydrogen storage tanks that have been developed so far are mainly based on metal hydrides (MHs) due to their increased gravimetric/volumetric capacity, as well as their stability, in some cases, over longterm cycling [1,2].

Hydrogen storage in MHs is an exothermic process that produces significant excess heat (in the range of 20–80 kJ/mol H_2 for common materials), as atomic hydrogen is bound chemically into the bulk of the material. Unless this produced excess heat is removed, it leads to increasing tank temperatures that eventually satisfy the activation energy barrier for desorption. As such, the material can no longer absorb more

---

[*] *Corresponding author*. Tel.: +30 210 6503408; fax: +30 210 6525004.
E-mail address: yiotis@ipta.demokritos.gr (A.G. Yiotis).

http://dx.doi.org/10.1016/j.ijhydene.2015.05.186

hydrogen resulting in incomplete fillings. The design of efficient cooling systems for MH tanks is thus a crucial factor in order to take advantage of the maximum storage capacity of the material [3]. Hydrogen desorption, on the other hand, is an endothermic reaction that requires sufficient heat fluxes to be provided to the MH tank in order to maintain the desired desorption mass fluxes needed to run a FC.

Recent studies have investigated the possibility to develop integrated, thermally-coupled MH tank/FC systems, where the thermal power produced in the FC during H_2 oxidation (that would be otherwise rejected to the environment) is redirected towards the MH tank in order to sustain H_2 desorption without the need for external heating sources, thus significantly increasing the overall system power efficiency. These works focus primarily on the thermal coupling between Proton Exchange Membrane FCs (PEMFCs) with low-temperature AB2 and AB5-type MHs (with low H_2 capacity) using convective heat transfer (air-cooling) and natural convection [4–6]. Other studies have addressed the problem of H_2 desorption from MgH_2 tanks, that offer increased storage capacity at the cost of very high desorption temperatures, heated by either the combustion of unused H_2 off-gas [7], or radiation from the external walls of a Solid Oxide FC (SOFC) [8]. A limited amount of research has also been devoted to the experimental study of the thermal coupling of High Temperature PEMFCs (HT-PEMFC) with complex hydrides, such as sodium alanates [9,10].

These studies have demonstrated that the dominant heat transfer mechanism in such coupled systems strongly depends on both the typical operating specifications of the FC, as well as the thermodynamic stability (through the associated enthalpy for H_2 desorption) and the desorption kinetics (through the activation energy) of the MH used. The typical operating temperature of a FC, T_{fc}, is primarily a function of the composition of the ion conducting membrane that separates the anode and cathode porous electrodes and the basic electrochemical reactions occurring at the Membrane Electron Assembly (MEA). In the case of PEMFCs, for example, where the electrodes are separated by a thin proton conducting membrane, e.g. Nafion, optimal power production is obtained in the range $50\ ^\circ C < T_{fc} < 100\ ^\circ C$. For SOFCs on the other hand, the membrane is composed of a ceramic material, conducting oxygen ions at temperatures well above $T_{fc} > 600\ ^\circ C$. This wide range of FC operating conditions has a profound impact on the selection of the MH component for the coupled system.

Apparently, the MH for the integrated system should be selected so that it bears both sufficiently fast desorption kinetics at a temperature several degrees lower than T_{fc}, but also a sufficiently high pressure Van't Hoff plateau, so that the tank satisfies the inlet H_2 pressure requirements for normal FC operation. In addition care must be taken to attain the required heat fluxes to maintain steady state desorption conditions. The latter is proportional to the H_2 desorption enthalpy of the MH and the H_2 mass flux required from the FC specifications. For the case of lower temperature PEM fuels cells ($T_{fc} < 100\ ^\circ C$), convective air cooling can be used to remove excess FC heat and maintain constant desorption rates at the MH tank [6]. For higher temperature applications though, using e.g. HT-PEMFCs, where the humidified exhaust gases act as a strong oxidizing agent for the metal parts of the integrated system, thermal liquids can be used instead for more efficient heat transfer [3].

In the present work, we address the latter case, where a HT-PEMFC is thermally coupled with a medium temperature MH tank, containing Ti-doped sodium alanate ($NaAlH_4$). This is considered a prototype H_2 solid-state storage material [11], after the pioneering work of Bogdanović et al. [12], demonstrating that it can reversibly store H_2 in the technologically favorable range of moderate temperatures below 160 °C. Since then, sodium alanate has been the subject of intense research which allowed the design, construction and testing of real alanate hydride storage tanks up to kg-scale using different well-characterized forms of the material (catalyzed, compacted, mixed with conduction enhancers etc) [11,13].

A material like sodium alanate can be ideally combined with a HT-PEMFC, that exhibits distinct advantages over classic PEMFCs, namely lower activation overpotentials, better electrochemical kinetics, improved water management and higher quality of exhaust thermal power due to its increased operating temperature range, $110\ ^\circ C < T < 180\ ^\circ C$ [14,15]. In our approach we propose a configuration where the thermal power required for H_2 desorption in the sodium alanate tank is provided from the HT-PEMFC using a heat transfer fluid that flows in a closed-circuit between them. The excess heat is recovered from the FC by air-cooling the FC cathode with an excess of air [16]. Assuming a typical tubular geometry for both the MH tank and the FC, we solve numerically a physical model that accounts for heat transfer in all the components of the integrated system and H_2 desorption kinetics and flow in the tank.

Integrated system design

We consider a tubular sodium alanate tank with an inner radius $R = 0.05$ m and variable length L [17,13]. The tank is surrounded by a heating jacket with thickness, $d = 0.01$ m, where a commercially available transfer fluid (Downtherm T by Dow Chemicals) is flowing normal to the axial direction of the tank (cross-flow). The thermal fluid redirects the heat produced in a HT-PEMFC towards the walls of the sodium alanate tank in a closed-circuit configuration, as shown in Fig. 1. Without loss of generality, we assume that the FC has also a typical tubular geometry with the same dimensions as the MH tank. We note here that the generic physical model presented below can be applied to more elaborate and realistic system designs.

We assume that a fixed H_2 molar flow rate, $\dot{n}_{H_2}$, is extracted from the MH tank (by imposing an appropriate boundary condition at the MH tank walls) and is then supplied to the FC anode through a thermally insulated pipe at the current average temperature of the tank, T_{MH}, which is a dependent variable in our study. At the same time, air is introduced at the cathode of the FC at environmental temperature, T_{env}, and at a fixed flow rate, $\dot{n}_a = \dot{n}_{O_2} + \dot{n}_{N_2} = 2.5\beta\dot{n}_{H_2}$, where $\dot{n}_{O_2}$, $\dot{n}_{N_2}$ are the molar flow rates of O_2 and N_2, respectively, and $\beta \geq 1$ is the excess of injected air flow. For $\beta = 1$ the reactants are in stoichiometric proportions. The excess of air provides a direct method for controlling the operating temperature of the FC by

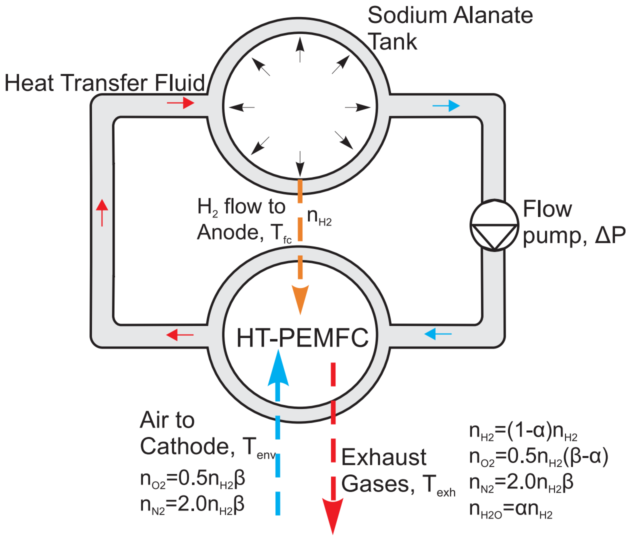

Fig. 1 – Schematic of the thermally-coupled closed-circuit system. Both the sodium alanate tank (top) and the High-Temperature PEMFC (bottom) are considered tubular with the same diameter. H_2 is desorbed from the tank at a fixed mass flux, $\dot{n}_{H_2}$ and an average temperature T_{MH}, and is supplied to the FC anode. Part of the thermal power produced during H_2 oxidation is recovered from the heat transfer fluid that flows in the surrounding heating jacket and redirected to the tank to maintain desorption. An excess of air, β, is injected to the FC cathode in order to recover the remaining thermal power and maintain a steady state operating temperature.

rejecting to the ambient the unused thermal power of the FC, as commonly practiced in commercial FCs [18,16].

The supplied H_2 is then oxidized in the FC producing electrical and thermal power, as will be discussed in more detail in section 6. Part of the thermal power is recovered by the heat transfer fluid that flows within the heating jacket surrounding the FC and is transferred to the MH tank, in order to maintain the tank temperature within an operationally favorable range, where the endothermic desorption kinetics are sufficiently fast to produce the required mass fluxes of H_2. The proposed H_2 storage-use system is thus fully coupled, with the HT-PEMFC providing heat towards the MH tank (by means of the heat transfer fluid), which in turn produces H_2 to maintain a steady-state HT-PEMFC operation. The thermal power produced in the FC is proportional to the incoming H_2 mass flux.

The numerical modeling of such a fully-coupled system requires the solution of the heat transfer problem in all system components (tank, FC, heating jacket) including heat production and consumption in the FC and the MH tank, respectively, and H_2 desorption kinetics and flow within the tank. We thus assume that the integrated MH Tank - FC system comprises of three distinct components;

1. The *MH tank*, where we solve for H_2 production based on the kinetics of the desorption reaction and the applied mass flux conditions at the tank walls, for H_2 flow through the porous MH bed, and for heat transfer and consumption due to endothermic desorption reaction.
2. The *HT-PEMFC*, where we solve for conductive heat transfer and production due to the exothermic oxidation reaction and the heating of the reacting and inert components. We also account for the heat carried by the exhaust gases (reaction products, unused reactants and inert species) that, depending on their temperature, affects the heat balance in the FC.
3. The *heating jacket* containing a heat transfer fluid that flows between the MH tank and the FC, and where we solve for flow and heat transfer assuming continuity boundary conditions at the FC and MH tank walls.

The governing equations for each component are discussed in detail in the following sections.

Sodium alanate desorption kinetics in the MH tank

The MH bed consists of a Ti-doped $NaAlH_4$ powder with porosity, ε, and permeability, k, as shown in Table 1. It has been shown that sodium alanate produces hydrogen following a two-step endothermic reaction involving the

Table 1 – Physicochemical system properties.

MH tank: sodium alanate and bed properties [26,23,27,22]	
Pure sodium alanate density, $\rho_{s1,sat}$	1240 kg/m^3
Molecular weight, M_{s1}	54 kg/kmol
Specific heat capacity of bed, C_{pb}	1075 J/kg/K
Thermal conductivity, K_s	0.5 W/m/K
Bed permeability, k	10^{-8} m^2
Bed porosity, ε	0.5
Enthalpy of desorption for Step 1, ΔH_{s1}	37 kJ/mol H_2
Entropy of desorption for Step 1, ΔS_{s1}	122 J/K/mol H_2
Enthalpy of desorption for Step 2, ΔH_{s2}	47 kJ/mol H_2
Entropy of desorption for Step 2, ΔS_{s2}	126 J/K/mol H_2
Activation energy for Step 1, E_1	105.85 kJ/mol
Reaction rate prefactor for Step 1, A_1	5.41×10^{10}/s
Activation energy for Step 2, E_2	91.50 kJ/mol
Reaction rate prefactor for Step 2, A_2	3.41×10^{8}/s
Hydrogen properties	
Density, ρ_g	P_gM_g/RT
Viscosity, μ_g	Sutherland formula
Molecular weight, M_g	2 kg/kmol
Enthalpy of oxidation, ΔH_{ox}	−250 kJ/mol H_2
Gibbs free energy of oxidation, ΔG_{ox}	−228 kJ/mol H_2
DOWNTHERM T heat transfer fluid properties @140 °C	
Density, ρ_f	790.6 kg/m^3
Viscosity, μ_f	1.45×10^{-3} Pa·s
Specific heat capacity, C_{pf}	2320 J/kg/K
Thermal conductivity, K_f	0.11 W/m/K
Fuel cell properties	
Density, ρ_{fc}	7850 kg/m^3
Specific heat capacity, C_{pfc}	475 J/kg/K
Thermal conductivity, K_{fc}	44.5 W/m/K
Fuel cell efficiency, ν	$0.5\lvert\Delta G_{ox}/\Delta H_{ox}\rvert$
Fuel utilization ration, α	0.80

production of intermediate species, such as Na_3AlH_6 and NaH [19,1];

$$NaAlH_4 \rightarrow \frac{1}{3}Na_3AlH_6 + \frac{2}{3}Al + H_2 + \Delta H_{s_1} \tag{1}$$

$$Na_3AlH_6 \rightarrow 3NaH + Al + \frac{3}{2}H_2 + \Delta H_{s_2} \tag{2}$$

where the corresponding reaction enthalpies are both ΔH_{s1} and $\Delta H_{s2} > 0$.

In principle, only 75% w/w of the overall H_2 stored in sodium alanate can be recovered following the above two-step reaction that exhibits satisfactory fast desorption kinetics in the range of $100\ ^\circ C < T < 160\ ^\circ C$ when doped with Ti-based compounds [19,12], thus yielding a 5.5% w/w usable H_2 storage capacity [20]. Further dehydration of the produced NaH occurs at significantly higher temperatures, well above 400 °C, thus rendering the remaining H_2 unrecoverable for common technological applications [1].

The reaction kinetics of each of the above steps in Ti-doped systems have been studied experimentally and independently at different pressure and temperature conditions, where either Na_3AlH_6 is the most stable species, thus favoring only the first step, or where NaH is the most stable species, thus favoring only the second step [21,22].

The kinetics of the first step can be adequately described by a zero-order reaction as follows [21,22];

$$\frac{da_{s_1}}{dt} = -k_1(p,T) \Rightarrow \frac{dc_{s_1}}{dt} = -k_1(p,T)c_{s_1,sat} = m_1 \leq 0 \tag{3}$$

where $a_{s_1} = c_{s_1}/c_{s_1,sat}$ is the fraction of $NaAlH_4$ molar concentration per bed volume, c_{s1}, over the initial fully saturated concentration, $c_{s1,sat}$.

The rate constant k_1 is a function of temperature, through the Arrhenius equation, and H_2 pressure in the void (otherwised referred to as 'back-pressure'), that limits the apparent desorption rate, as follows;

$$k_1 = A_1 e^{\frac{E_1}{RT}}(\Delta P_1 + 1.04\Delta P_1) \tag{4}$$

where $\Delta P_1 = p_{eq,1} - p/p_{eq,1}$ and the equilibrium pressure, $p_{eq,1}$, is obtained by the Van't Hoff equation;

$$\ln\left(p_{eq,1}\Big/p_0\right) = -\Delta H_{s_1}/RT + \Delta S_{s_1}/R \tag{5}$$

where p_0 is the atmospheric pressure. In the above equations ΔH_{s1} and ΔS_{s1} is the standard enthalpy and entropy change of the reaction, respectively, E_1 is the activation energy, A_1 is a rate prefactor, T is the temperature and R is the ideal gas constant. The values of the above properties are shown in Table 1.

The kinetics of the second reaction step can be described by a first-order reaction as follows [21,22];

$$\frac{da_{s_2}}{dt} = -k_2(p,T)a_{s_2} \Rightarrow \frac{dc_{s_2}}{dt} = -k_2(p,T)c_{s_2} = m_2 \leq 0 \tag{6}$$

where $a_{s_2} = c_{s_2}/c_{s_2,sat}$ is the fraction of Na_3AlH_6 molar concentration per bed volume, c_{s2}, normalized by the maximum molar concentration of Na_3AlH_6 that could be obtained by the first step of the reaction, namely $a_{s_2} = c_{s_2}/c_{s_2,max} = 3c_{s_2}/c_{s_1,max}$. The rate constant k_2 is also a function of temperature and H_2 back-pressure as follows;

$$k_2 = A_2 e^{\frac{E_2}{RT}}\left(\Delta P_2^2 - 0.46\Delta P_2\right) \tag{7}$$

where $\Delta P_2 = p_{eq,2} - p/p_{eq,2}$ and the equilibrium pressure, $p_{eq,2}$, is obtained by the Van't Hoff equation;

$$\ln\left(p_{eq,2}\Big/p_0\right) = -\Delta H_{s_2}/RT + \Delta S_{s_2}/R \tag{8}$$

where ΔH_{s2} and ΔS_{s2} are the standard enthalpy and entropy change of the reaction, respectively, E_2 is the activation energy and A_2 is a rate prefactor (see Table 1).

In the general case when both steps occur simultaneously, the mass balances for $NaAlH_4$ and Na_3AlH_6 read, respectively;

$$\frac{\partial c_{s_1}}{\partial t} = -k_1 c_{s_1,sat} = m_1 \tag{9}$$

$$\frac{\partial c_{s_2}}{\partial t} = -k_2 c_{s_2} + \frac{1}{3}k_1 c_{s_1,sat} = m_2 - \frac{1}{3}m_1 \tag{10}$$

The above reaction kinetics are solved in the MH tank starting from an initially fully saturated medium, namely when $c_{s1} = c_{s1,sat}$ and $c_{s2} = 0$.

Heat transfer and H_2 flow in the MH tank

Considering a tubular sodium alanate tank, where H_2 is released from one or both ends of the tank towards the HT-PEMFC, it is reasonable to assume that the process of heat transfer and H_2 flow is controlled by transport in the radial (from the heated tank walls towards the center of the tank), rather than the axial direction (along the top and bottom sides of the tank). This is due to the combined effect of the higher bed porosity closer to the tank walls (resulting from the packing process when the tank is filled with sodium alanate powder or packed pellets [13]), that allows for easier H_2 flow along the inner tank walls towards the top and bottom valves, as well as the significantly higher temperature gradients in the radial direction (as the tank walls are uniformly heated from the flowing fluid), leading to faster desorption kinetics, and thus concentration gradients in the same direction. This approach significantly simplifies the numerical modeling of the problem as it reduces to a 2D equivalent, where we assume that the desorbed H_2 flows through the porous bed towards the tank walls. We impose there a fixed molar flux per unit tank length, $\dot{n}_{H_2}$, that is subsequently supplied to the FC in order to maintain a constant electrical power production, P_e. The mass balance for H_2 in the gaseous phase (void space) then reads;

$$\varepsilon\frac{\partial \rho_g}{\partial t} + \nabla\cdot\left(\rho_g\langle\vec{u}_g\rangle\right) = -\left(m_1 + \frac{3}{2}m_2\right)M_g \tag{11}$$

where $\langle\vec{u}_g\rangle$ is the Darcy velocity of the gaseous phase;

$$\langle\vec{u}_g\rangle = -\frac{k}{\mu_g}\nabla P_g \tag{12}$$

P_g, ρ_g, M_g are the H_2 pressure, density and molar weight, respectively (see Table 1). μ_g is the viscosity of H_2 with a temperature dependence calculated by Sutherland's formula $\mu_g = \mu_0\left(\frac{T_0+C}{T+C}\right)(T/T_0)^{3/2}$, $C = 72$ K, $T_0 = 293.85$ K, $\mu_0 = 8.76\times10^{-6}$Pa·s.

For heat transfer, we consider the MH bed as a homogeneous and isotropic effective continuum, where the thermal properties are averaged over the entire solid and void space, and convective heat transfer is neglected;

$$\rho_b C_{pb}\frac{\partial T}{\partial t} + \nabla\cdot(-K_e\nabla T) = m_1\Delta H_{s_1} + \frac{3}{2}m_2\Delta H_{s_2} \tag{13}$$

where $\rho_b = \varepsilon\rho_{s1,sat} = c_{s1,sat}M_{s1}$ is the bed density, C_{pb} is the bed specific heat capacity, K_e is the effective thermal conductivity and M_{s1} is the molar weight of sodium alanate.

In the present study, we assume that the thermal properties and the porosity of the bed remain constant throughout the desorption process, regardless of the chemical composition of the bed (namely, the fraction of $NaAlH_4$, Na_3AlH_6 and NaH), given that all species have approximately similar properties [23]. The effects of compositional changes on tank properties during desorption have been addressed in previous works [24,8].

Flow and heat transfer in the heating jacket

As discussed earlier, both the FC and the MH tank are covered by a heating jacket, where a thermal fluid transfers heat between them, in order to partially cool the FC, and at the same time provide heat to maintain H_2 desorption in the MH tank. Heat transfer through the metal tank walls is assumed to be infinitely fast due to the significantly higher thermal conductivity of the material compared to those of the MH bed and the heating fluid (a difference that could be as high as two orders of magnitude). We thus assume that the process is controlled by heat transfer in the liquid and the MH bed, neglecting any thermal resistance at the walls.

Within the heating jacket we solve the incompressible Navier–Stokes and continuity equations to calculate the flow field of the heat transfer fluid;

$$\rho_f\left(\frac{\partial\vec{u}_f}{\partial t} + \vec{u}_f\cdot\nabla\vec{u}_f\right) = -\nabla p + \mu_f\nabla^2\vec{u}_f \tag{14}$$

where $\vec{u}_f$, p, μ_f, ρ_f are the heating fluid velocity, pressure, viscosity and density, respectively, and;

$$\nabla\cdot\vec{u}_f = 0. \tag{15}$$

The flow field is then coupled with a heat balance to calculate the temperature profile in the heating jacket and the heat fluxes across the tank and FC walls;

$$\rho_f C_{pf}\frac{\partial T}{\partial t} + \nabla\cdot\left(\rho_f\vec{u}_f C_{pf}T - K_f\nabla T\right) = 0 \tag{16}$$

where C_{pf} and K_f are the fluid specific heat capacity and thermal conductivity, respectively (see Table 1).

We couple the solution for the temperature in the MH tank by considering continuity of heat fluxes and temperature at the MH tank walls;

$$\vec{n}\cdot\left(K_f\nabla T|_{S_{MH+}} - K_e\nabla T|_{S_{MH-}}\right) = 0 \text{ and } T_{S_{MH+}} = T|_{S_{MH-}} \tag{17}$$

where $\vec{n}$ is the unit vector normal to the surface, S_{MH}, of the MH tank walls.

Thermal power production in the PEM fuel cell

FCs are electrochemical devices that efficiently convert the Gibbs free energy, associated with H_2 oxidation, to electrical work. As shown in previous publications [25,16], joule heating within the FC components (membrane, porous electrodes) is the primary source of energy dissipation at peak electrical power, yielding a typical electrical system efficiency equal to $\nu = 0.5|\Delta G_{ox}/\Delta H_{ox}|$, where ΔG_{ox} and ΔH_{ox} are the Gibbs free energy and enthalpy of H_2 oxidation at the FC operating temperature [8]. The remaining energy is dissipated to thermal power that should be efficiently removed from the fuel cell in order to maintain a constant operating temperature, T_{fc}, and avoid overheating that could damage the MEA.

The thermal power produced in the FC due to hydrogen oxidation and joule heating in the MEA components can be thus expressed in terms of the H_2 utilization ratio, α (the ratio of reacting over the total number of moles of H_2 supplied to the FC anode), and molar flow rate per unit tank length, $\dot{n}_{H_2}$, as;

$$\dot{q}_{ox} = \alpha(1-\nu)\dot{n}_{H_2}|\Delta H_{ox}| \tag{18}$$

Part of this power is used for heating the reacting and inert species, air and H_2, to the FC operating temperature (see Fig. 1). This thermal power can be calculated as a function of the molar flow rates, $\dot{n}_{O_2}$, $\dot{n}_{N_2}$, for O_2 and N_2, respectively, (where $\dot{n}_{N_2} = 4\dot{n}_{O_2}$) and the corresponding temperatures of the flow streams, the average MH tank temperature, T_{MH}, for H_2, and the ambient temperature, T_{env} for air species;

$$\dot{q}_{heat} = \dot{n}_{H_2}\int_{T_{MH}}^{T_{fc}} c_{p,H_2}\,dT + \dot{n}_{O_2}\int_{T_{env}}^{T_{fc}} c_{p,O_2}\,dT + \dot{n}_{N_2}\int_{T_{env}}^{T_{fc}} c_{p,N_2}\,dT \tag{19}$$

where $c_{p,i}$ is the mole specific heat capacity under constant pressure of component i.

The above can be further simplified in terms of the H_2 flow rate by considering the stoichiometry of the reaction and an excess β of air flow rate, where $\beta \geq 1$;

$$\dot{q}_{heat} = \dot{n}_{H_2}\left(\int_{T_{MH}}^{T_{fc}} c_{p,H_2}\,dT + 0.5\beta\int_{T_{env}}^{T_{fc}} c_{p,O_2}\,dT + 2\beta\int_{T_{env}}^{T_{fc}} c_{p,N_2}\,dT\right) \tag{20}$$

Note that for $\beta = 1$, the reactants are in stoichiometric analogy, and thus the exhaust flow stream contains only the inert species, i.e. N_2, and the products, i.e. H_2O.

Assuming that the exhaust gases exit from the FC at a temperature, $T_{exh} \leq T_{fc}$, then part of the thermal power carried by the overheated exhaust gases remains in the FC;

$$\dot{q}_{exh} = \dot{n}_{H_2}\int_{T_{fc}}^{T_{env}}\left[(1-\alpha)c_{p,H_2} + 0.5(\beta-\alpha)c_{p,O_2} + 2\beta c_{p,N_2} + \alpha c_{p,H_2O}\right]dT \leq 0 \tag{21}$$

When $T_{exh} = T_{fc}$, the total thermal power carried by the exhaust gases is rejected to the environment. This is the typical case considered in this study.

The residual thermal power per unit tank length produced in the FC, that can be recovered by the closed-circuit heat transfer fluid, is then;

$$\dot{q}_{fc} = \dot{q}_{ox} - \dot{q}_{heat} - \dot{q}_{exh} \tag{22}$$

In our approach, we assume that the above thermal power is homogeneously generated over the entire FC volume, which is made of a highly conductive material, i.e. steel. A more elaborate study of heat transfer and production within the FC would consider the actual geometry and heat transfer properties of individual MEA components, which is however beyond the aim of the present work.

We thus solve for heat transfer in the FC as follows;

$$\rho_{fc} C_{pfc} \frac{\partial T}{\partial t} - K_{fc} \nabla^2 T = \dot{q}_{fc} \Big/ V_{fc} \tag{23}$$

where V_{fc} is the volume of the FC per length unit, assuming continuity of heat fluxes and temperature at the FC walls;

$$\vec{n} \cdot \left(K_f \nabla T \big|_{S_{fc}+} - K_{fc} \nabla T \big|_{S_{fc}-} \right) = 0 \text{ and } T|_{S_{fc}+} = T|_{S_{fc}-} \tag{24}$$

where $\vec{n}$ is the unit vector normal to the surface, S_{fc}, of the HT-PEMFC walls.

We note here that heat production in the FC, $\dot{q}_{fc} = \dot{q}_{fc}(\dot{n}_{H_2})$, is directly coupled with the H_2 molar flow rate from the MH tank, which in turn depends on heat production in the FC and heat transfer dynamics in the heating jacket.

Results and discussion

The above physical model is solved using a commercial finite element solver, COMSOL Multiphysics 4.3. A series of numerical simulations in the coupled MH-FC system are performed in order to study the typical operating conditions (temperature and MH tank pressure) at typical HT-PEMFC ratings. For simplicity and without loss of generality, we design a 2D system where the MH tank and the HT-PEMFC are placed in series and interconnected with a straight heating jacket as shown in Fig. 2. We apply a pressure difference, $\Delta P = P_{in} - P_{out}$, and periodic thermal conditions, $T_{in} = T_{out}$ and $\vec{n} \cdot (K_f \nabla T|_{in} - K_f \nabla T|_{out}) = 0$, at the ends of the heat transfer fluid channels to model a closed-circuit flow driven by a pump located between the two ends (not shown in the figure).

As discussed also earlier, we assume in our approach that the gradients of temperature and pressure within the MH tank are negligible in the axial compared to the radial direction of the tank, and it is thus sufficient to solve for a 2D cross-section of the system as shown in Fig. 2. Furthermore, we only solve for the top half of the system, assuming a plane of symmetry between the upper and lower parts, where we impose no-flux boundary conditions.

We allow the system to reach a steady state for an initial period of 10 mins when the temperature is uniformly set to an initial value of $T_0 = 130\,^\circ C$ and the H_2 pressure in the tank is set to its corresponding equilibrium value (see Eqs.(5) and (8)). During this time, the MH tank valve is closed, namely there is no H_2 flow towards the FC, and thus no electrical and thermal power generated in the FC. We then gradually increase the flow rate from the MH tank to the FC anode until a maximum value of $\dot{n}_{H_2} = P_e/(\nu\alpha|\Delta H_{ox}|)$, that produces P_e electrical power per tube unit length. At the same time, air is injected to the FC cathode at a flow rate equal to $\dot{n}_a = 2.5\beta\dot{n}_{H_2}$, and electrical and thermal power production begins in the HT-PEMFC.

The system operates at the fixed imposed electrical power, P_e, until the MH tank becomes either concentration or pressure depleted, whichever condition is satisfied first. In the first case, there is no more hydrogen left to desorb from the reactants (either $NaAlH_4$ or Na_3AlH_6), and therefore the reactions terminate. The maximum usable energy (both thermal and electrical) contained in the tank per unit length is;

$$E_{max} = \frac{3}{2} \frac{\rho_{s_1} \varepsilon V}{M_{s_1}} |\Delta H_{ox}| \tag{25}$$

Therefore, the maximum operation time until the tank becomes concentration depleted is;

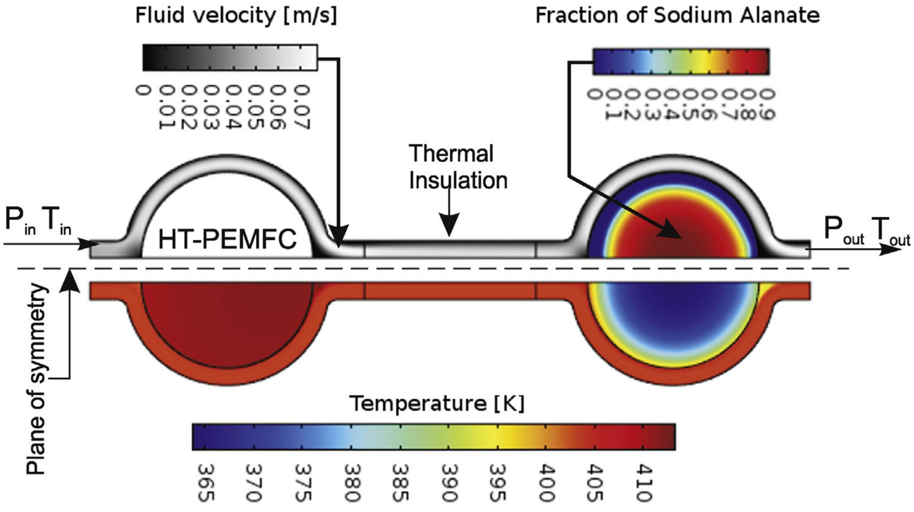

Fig. 2 – Typical temperature, velocity and $NaAlH_4$ fraction profiles of the 2D computational domain for a simulation at $P_e = 800$ W/m and $\beta = 12$ after 2 h of operation. The computational domain is constructed in such a way in order to take advantage of the plane of symmetry that passes from the center of the tank and the FC.

$$t_{max} = \frac{E_{max}}{\dot{n}_{H_2}|\Delta H_{ox}|} = \frac{3}{2}\alpha\nu\frac{\rho_{s_1}\epsilon V|\Delta H_{ox}|}{M_{s_1}P_e}, \tag{26}$$

which for a fixed electrical power of $P_e = 1000$ W/m, equals to $t_{max} = 3.38$ h. This operation time however is never achieved due to heat transfer limitations, that lead to the cooling of the tank at temperatures, where the desorption kinetics are poor and thus cannot satisfy the applied mass flow rate demand. Eventually, the tank becomes pressure depleted, while significant amounts of H_2 still remain in the form of $NaAlH_4$ and/or Na_3AlH_6. From this point onwards, we assume that the tank becomes pressure depleted, namely can no longer satisfy FC operating specifications, when the average H_2 pressure drops below 10^5 Pa.

As also discussed earlier, only a part of the thermal power produced during H_2 oxidation in the FC is required for maintaining H_2 desorption in the MH tank. Based on the reaction enthalpies and the stoichiometry of the two desorption steps (see Eqs. (1)–(2)), the mass weighted average energy consumed for desorption is approximately equal to 40.3 kJ/mol H_2. This is much lower than the total thermal energy produced in the FC, which can be found approximately equal to 110 kJ/mol H_2 as shown in section 6. The remaining power should be efficiently removed from the system by providing an excess of atmospheric air, β, in the fuel cell cathode, that serves as a cooling medium for the system. By solving Eqs. (18)–(22) assuming typical operating conditions, we find that an excess of air, approximately equal to $\beta \approx 12$, is sufficient to maintain a steady state temperature at the FC, namely the heat flow rate recovered by the heat transfer fluid is sufficient to maintain H_2 desorption in tank. This air-cooling approach is typically applied in commercial FCs [16].

Sodium alanate tank desorption dynamics

Fig. 3 shows a time series of concentration and temperature profiles in the sodium alanate tank for a typical simulation at $P_e = 800$ W/m. The fraction of $NaAlH_4$ (top) changes progressively with time from a fully saturated value to zero, starting from bed areas closer to the tank walls, where the medium temperature is higher (see temperature series in the bottom) and the desorption kinetics are thus faster. This eventually results in the development of a reaction front that progressively moves towards the center of the tank, leaving behind a concentration depleted area. As temperature gradients in the radial direction remain constant to compensate for heat consumption in the endothermic H_2 desorption reaction, the heat fluxes provided by the circulation of the heating fluid have to travel through this bed region to reach the receding reaction front, thus resulting in progressively lower temperatures in the frontal region (where the reaction actually takes place).

At early times, the fraction of the intermediate species, Na_3AlH_6, which is consumed in the second reaction step, appears to be approximately constant within the frontal region of the first reaction step, while it has a zero value on both sides across it, towards the walls and the center of tank (Fig. 3-(middle)). This implies that at early times the first reaction step is controlling the desorption process, despite the higher thermodynamic stability, $\Delta H_{s2} > \Delta H_{s1}$, of Na_3AlH_6 compared to $NaAlH_4$. At later times, however, when the temperature in the tank drops below a critical value, as shown in Fig. 3-(bottom), there is a significant accumulation of Na_3AlH_6 in the frontal region, indicating possible poor kinetics of the second step at this stage.

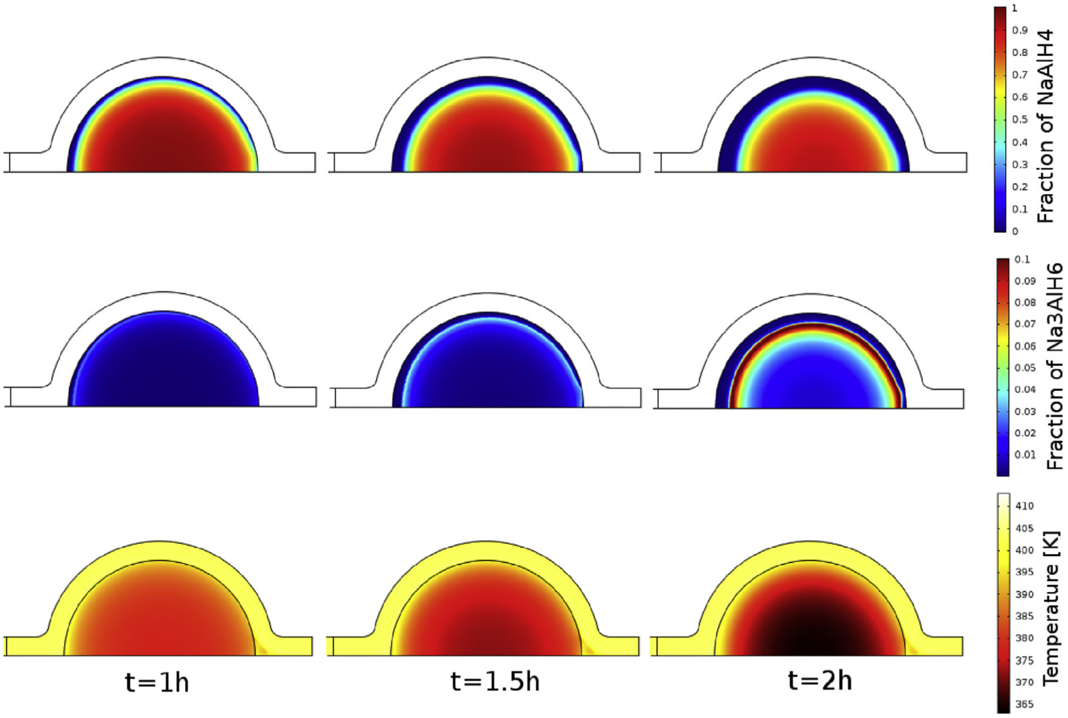

Fig. 3 – Concentration and temperature profiles in the sodium alanane tank at different times of system operation at $P_e = 800$ W/m. (top) – Fraction of $NaAlH_4$ at 1, 1.5 and 2 h (from left to right) of desorption. (middle) – Fraction of Na_3AlH_6 at the same times. (bottom) – Temperature profiles at the same times.

This effect is further demonstrated in Fig. 4 that shows the fraction of the two species, $NaAlH_4$ (left) and Na_3AlH_6 (right), with time for three simulations at different values of P_e. Initially, the slope of the $NaAlH_4$ reaction is constant and a function of P_e, namely higher values of P_e lead to larger slopes. At the same time, the fraction of Na_3AlH_6 remains practically constant with time, exhibiting a low value plateau. At later times, however, there is an exponential increase of the Na_3AlH_6 fraction due to poor reaction kinetics at lower temperatures in the reaction front region. The disruption of the second reaction step is followed by a further increase in the slope of the first step, as the imposed H_2 flux is now covered only by the first reaction.

The effects of poor thermal conductivity in the MH tank and the receding of the reaction front towards the center of the tank are also demonstrated in Fig. 5, that shows the dynamics of H_2 pressure in the tank for various values of P_e. The curves exhibit a sharp drop in pressure at very early times (when the tank valve is opened), followed by a relatively short steady-state period where the pressure is practically constant, corresponding to the development of the frontal reaction region adjacent to the external tank walls. This period is then followed by a sharp decrease in pressure corresponding to the receding of the front region and increasing resistance to heat transfer within the concentration depleted area. Eventually, the tank becomes pressure depleted although a large fraction of the available H_2 still remains absorbed. This is further shown in the inset of Fig. 5, where time has been rescaled with t_{max}, the time required to fully empty the tank at the current P_e. This plot shows the important effect of P_e on the operation time of the integrated system. For lower values of P_e, a significantly higher fraction of H_2 can be recovered before the tank becomes pressure depleted.

Temperature dynamics of the integrated system

An overview of the average temperature in the three distinct system components (FC, MH tank and heating jacket) is shown in Fig. 6 for two different values of P_e. A sharp decrease of the tank temperature is observed very early after the beginning of the desorption process, as the imposed H_2 flow rate drives the endothermic desorption reactions (given that they are thermodynamically feasible at the current initial temperature $T_0 = 130$ °C). During this early period the temperature gradients are still not sufficiently large to sustain heat fluxes, $\dot{q}_{tank,S} = \int_S (\vec{n} \cdot K_f \nabla T) dS$, from the heating jacket towards the tank, and thus the reactions progress by absorbing heat from the MH bed (leading to lower temperatures). The corresponding thermal power consumed by the two reaction steps is $\dot{q}_{reac,V} = \int_V (m_1 \Delta H_{s_1} + 3/2 m_2 \Delta H_{s_2}) dV$ (see Eq. (13)).

As a temperature gradient develops with time between the reaction front and the external tank walls, heat fluxes from the heating fluid become progressively larger, $\dot{q}_{tank,S}$, and a practically constant, steady-state, average tank pressure is achieved, that lasts 1.5 h in the case of $P_e = 500$ W/m (Fig. 6-(left)). This effect is also demonstrated in Fig. 7-(left), that shows the calculated heat flow rates across the tank walls and the average reaction power. Starting from an initial zero value, the heat flow rate quickly reaches a steady state value $\dot{q}_{reac,V} \approx -100$W/m. This is compensated by an equal amount of heat flow rate across the tank walls, $\dot{q}_{tank,S}$ that develops in response to the early stage temperature drop and the corresponding gradients of the temperature between the heating fluid and the tank.

Fig. 7 also shows the overall thermal power, $\dot{q}_{heat}$, required for heating the reacting and inert species to the operating temperature of the FC, as discussed in section 6. The thermal power, that is recovered from the heating fluid across the FC walls, $\dot{q}_{FC,S} = \int_S (\vec{n} \cdot K_f \nabla T) dS$, is found to be appropriately equal to $\dot{q}_{tank,S}$ at steady state operating conditions. Note that at steady state and when $\dot{q}_{exh} = 0$ (which is the case in our simulations), the sum of the above is equal to $\dot{q}_{ox} = \dot{q}_{heat} + \dot{q}_{FC,S} = \alpha(1-\nu)\dot{n}_{H2}|\Delta H_{ox}|$ (see Eqs. (18) and (22)). For $P_e = 500$ W/m, we thus find $\dot{q}_{ox} \approx 310$ W/m, as expected.

The steady state temperature period in Fig. 6 exactly matches the constant tank pressure period shown in Fig. 5, characteristic of the development of the reaction front adjacent to the tank walls. Similarly to the pressure dynamics plots, this period is followed by an almost linear decrease of

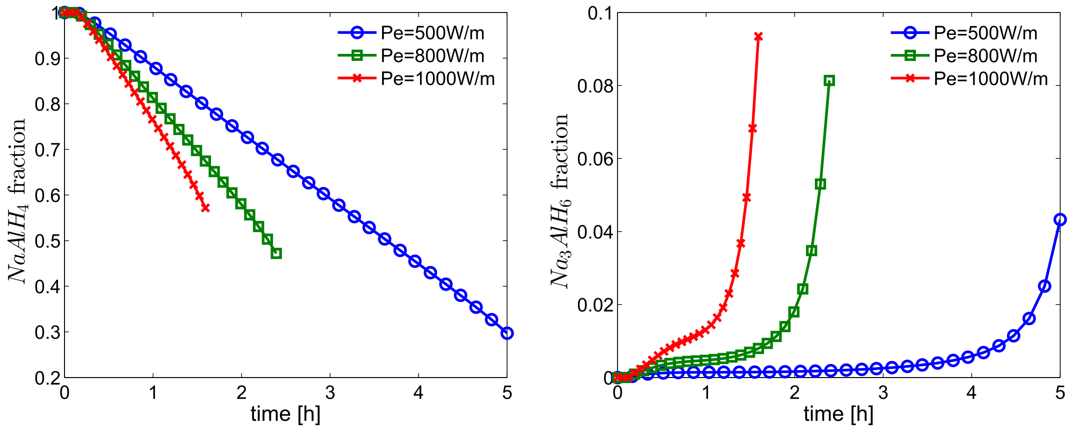

Fig. 4 – Average mass fraction of $NaAlH_4$ (left) and Na_3AlH_6 (right) in the MH tank for different values of the FC electrical power, P_e. At early to intermediate times of the process, and as long as the tank temperature is high enough, the $NaAlH_4$ desorption curve exhibits a constant slope which is proportional to P_e. At later times, when the tank temperature becomes sufficiently low, the kinetics of the second reaction step are unfavorable, leading to accumulation of Na_3AlH_6 and an increase (in absolute value) in the slope of the first reaction step in order to fulfill the fixed H_2 demand.

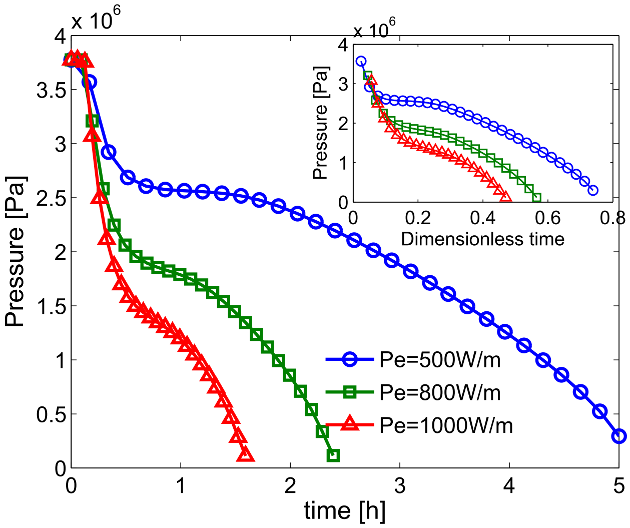

Fig. 5 – Average H_2 pressure in the MH tank during system operation for different values of the imposed electrical power on the FC. The inset shows the pressure vs the dimensionless time rescaled with the theoretical operating time of the system, t_{max}. For higher values of electrical power the tank becomes pressure depleted when only a fraction of the available energy has been recovered, e.g. only 50% at $P_e = 1000$ W/m compared to almost 80% at $P_e = 500$ W/m.

the average tank temperature, corresponding to the receding of the frontal region. It is interesting to note that the slope of the temperature curve becomes smoother during the very last stages of the process, when the second reaction step is blocked due to poor kinetics at low temperatures. This change of the slope should be attributed to H_2 production only from the first reaction step, which has a lower enthalpy of desorption compared to the second step, thus leading to smoother temperature time derivatives. Fig. 6 also shows that the average FC and heating fluid temperatures reach a steady state operation value, as long as the excess air fraction injected to FC cathode is sufficient to recover the remaining thermal power from the FC.

For completeness, we conclude our discussion by comparing our numerical results with the limited amount of experimental data available in the literature on such fully coupled systems. We focus on the findings of Urbanczyk et al. [10] who developed a comparable hydrogen storage system, comprising of a tubular sodium alanate tank doped with 4% mol/mol of $TiCl_3$ and a liquid cooled PBI-based HT-PEMFC stack. The tank of this study was approximately 0.5 long with an internal diameter of 0.2 m. A heat transfer oil, with comparable physical and thermal properties to the one of our study, was flowing through a sophisticated helicoidal piping system, running both within and around the body of the tank. The tank contained at total of 2.67 kg of sodium alanate with a volume equal to 5.1×10^{-3} m^3. Thus given the density of the pure material, the porosity of the bed can be estimated to be equal to $\varepsilon = 0.57$, very close to the value used in our study ($\varepsilon = 0.5$). Despite the more elaborate design of the heating piping, the tank can be directly compared to the one presented here given that they both contain approximately the same amount of sodium alanate per unit length (2.43 kg (our study) vs 2.67 kg (experimental study) for $L = 0.5$ m).

In the experimental study of Urbanczyk et al. [10], both the fuel cell and the sodium alanate tank are initially preheated up to their respective operating temperatures (~130 °C for the fuel cell and ~140 °C for the MH tank) using external heating sources. The heating oil circuit is then turned on and the system is tested over a specific load profile where the electrical power of the fuel cell is varied in the range of 160–240 W by appropriately adjusting H_2 flow from the MH tank, while monitoring the tank and fuel cell operating conditions. Neglecting the initial desorption period, when the tank temperature is actually higher than that of the fuel cell, it is rather interesting to compare the operational data after 2 h of system operation to our results for a fuel cell rating of $P_e = 500$ W/m, thus for an actual 250 W of electrical power taking a length of the tank equal to $L = 0.5$ m. The predicted tank pressure and temperature are approximately equal to 25 bar and 120 °C, respectively (Figs.(5)–(6)), in very good agreement with the values reported by Urbanczyk et al. [10] at the same fuel cell power ratings (20–30 bar pressure and an average temperature between 125–130 °C, using as a reference the oil temperature at the MH tank outlet). The experimental H_2 flow rate

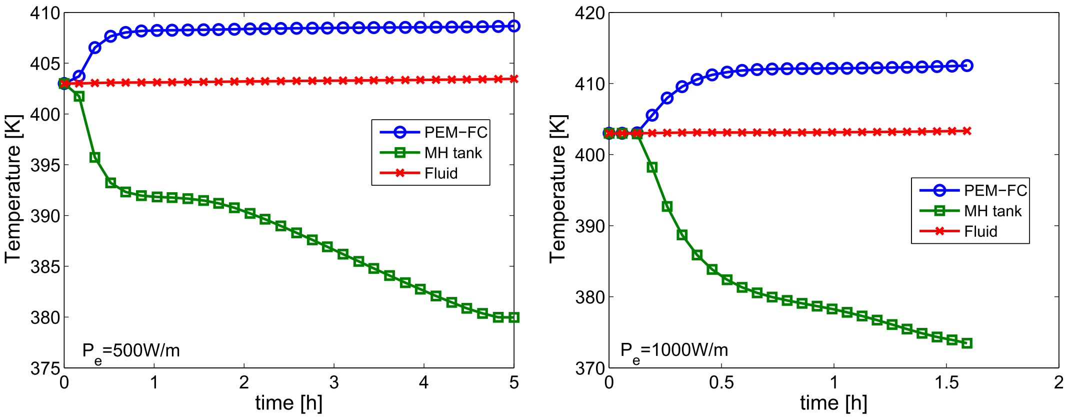

Fig. 6 – Overview of the average temperature in the system components (HT-PEMFC, MH tank and heat transfer fluid) vs time at $P_e = 500$ W/m (left) and $P_e = 1000$ W/m FC rating. A steady-state temperature at the FC is achieved for an excess of air at the cathode equal to $\beta \approx 12$.

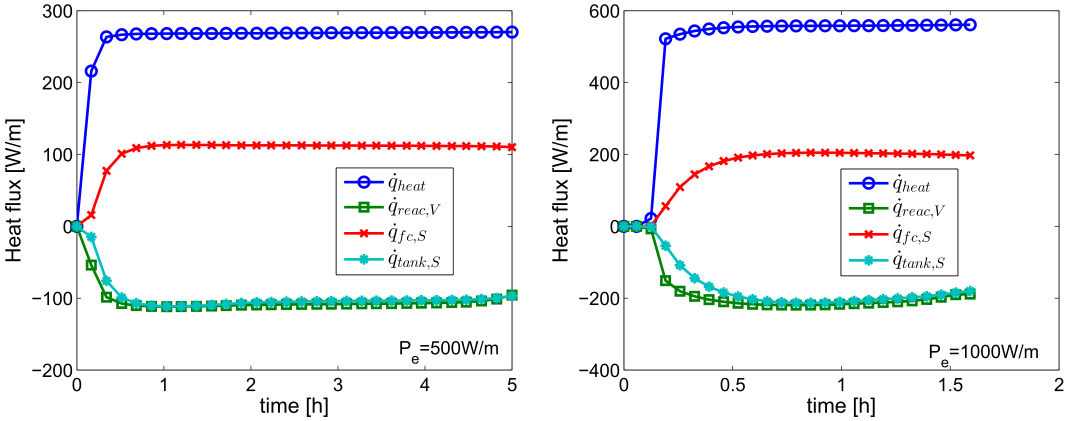

Fig. 7 – Heat fluxes across system components vs time at $P_e = 500$ W/m (left) and $P_e = 1000$ W/m FC ratings. $\dot{q}_{heat}$ is the thermal power recovered from the FC by heating the reacting and inert species. Also shown; the reaction power in the MH tank which is equal to $\dot{q}_{reac,V} = \int_V (m_1 \Delta H_{s_1} + 3/2 m_2 \Delta H_{s_2}) dV$ (see Eq. (13)), the thermal power across the FC walls towards the heating fluid, $\dot{q}_{fc,S}$, and the thermal power across the MH tank walls from the heating fluid towards the tank, $\dot{q}_{tank,S}$.

is reported to be equal to 255 Nl/h, in good agreement with the predicted 224 Nl/h of our model for a somehow lower fuel utilization ratio ($\alpha = 0.8$ compared to $\alpha = 0.84$ of the experiments), but for higher fuel cell efficiency ($\nu = 0.45$ compared to $\nu = 0.31$ of the experiments). The experimental air flow rate is approximately two times larger than the stoichiometrically required value, namely $\beta \approx 2$, which is significantly lower than the value reported in our study $\beta \approx 12$. This is however due to the significant heat loses to the ambient of the experimental infrastructure that compensate for the air-cooling of the fuel cell in the fully thermally insulated system of our study. Such effects however can be readily implemented in our physical model.

As a concluding remark, it is very interesting to note that only 60 g of H_2 (2.24% w/w), out of the maximum 89 g (3.35% w/w) storage capacity (experimentally determined following 14 absorption–desorption cycles), could be recovered from the above thermally coupled system, despite the elaborate design of the heating piping. This should be attributed to the pressure depletion of the tank (also evident in the pressure plots) that is a result of heat transfer limitations in the MH tank after prolonged system usage, as we have also observed in our simulations. This further demonstrates the need for design optimization in order to enhance heat transfer from the heating fluid towards the bulk of the MH tank, which can be readily realized with the physical model proposed in our study.

Conclusions

We proposed a generic physical model that describes the dynamics of a fully-coupled, thermally integrated high-temperature PEMFC and sodium alanate tank system. In our configuration, the thermal power required for H_2 desorption in the MH tank is recovered from the HT-PEMFC using a heat transfer fluid that flows in a closed-circuit between them. The thermal power is redirected towards the tank to maintain the endothermic H_2 reaction from sodium alanate. The remaining heat is then recovered from the FC by air-cooling the FC cathode with an excess of air.

The model accounts for heat transfer in all system components (tank, FC, heating jacket), including heat production and consumption in the FC and the MH tank, respectively, and H_2 desorption kinetics and flow in the tank. We show that the thermal power production in the FC can be conveniently partitioned between the MH tank and the exhaust gases, by fine tuning the excess of air injected at the FC, so that the heat fluxes towards the closed-circuit heating fluid exactly match the thermal power required for H_2 desorption in the tank. The model can thus be extended to any type of MH, provided that its desorption kinetics and thermodynamics are favorable in the operating temperature range of a HT-PEMFC.

Our simulations, using a simplified coupled system design, show that the poor thermal conductivity of the MH powder is the most important parameter of the problem, particularly at high electrical power ratings of the FC, that lead to faster pressure depletion of the tank due to kinetic limitations of the H_2 desorption reactions at lower tank temperatures, although the tank still contains large fractions of absorbed H_2. We demonstrate that our results compare quite favorably with the limited experimental data available on such coupled systems, showing that the proposed model can be applied in more elaborate system designs for optimization purposes.

Acknowledgments

This work is partially supported by the European Union under the H2FC program (FP7-Capacities, Grant Agreement Number 284522).

REFERENCES

[1] Orimo S-I, Nakamori Y, Eliseo JR, Züttel A, Jensen CM. Complex hydrides for hydrogen storage. Chem Rev 2007;107:4111–32.

[2] Sakintuna B, Lamari-Darkrim F, Hirscher M. Metal hydride materials for solid hydrogen storage: a review. Int J Hydrogen Energy 2007;32:1121–40.
[3] Bhouri M, Goyette J, Hardy B, Anton D. Numerical modeling and performance evaluation of multi-tubular sodium alanate hydride finned reactor. Int J Hydrogen Energy 2012;37:1551–67.
[4] Jiang Z, Dougal R, Liu S, Gadre S, Ebner A, Ritter J. Simulation of a thermally coupled metal-hydride hydrogen storage and fuel cell system. J Power Sources 2005;142:92–102.
[5] MacDonald BD, Rowe AM. Impacts of external heat transfer enhancements on metal hydride storage tanks. Int J Hydrogen Energy 2006a;31:1721–31.
[6] MacDonald BD, Rowe AM. A thermally coupled metal hydride hydrogen storage and fuel cell system. J Power Sources 2006b;161:346–55.
[7] Delhomme B, Lanzini A, Ortigoza-Villalba GA, Nachev S, de Rango P, Santarelli M, et al. Coupling and thermal integration of a solid oxide fuel cell with a magnesium hydride tank. Int J Hydrogen Energy 2013;38:4740–7.
[8] Yiotis A, Kainourgiakis M, Kosmidis Lefteris I, Charalambopoulou G, Stubos A. Thermal coupling potential of solid oxide fuel cells with metal hydride tanks: thermodynamic and design considerations towards integrated systems. J Power Sources 2014;269:440–50.
[9] Pfeifer P, Wall C, Jensen O, Hahn H, Fichtner M. Thermal coupling of a high temperature PEM fuel cell with a complex hydride tank. Int J Hydrogen Energy 2009;34:3457–66.
[10] Urbanczyk R, Peil S, Bathen D, Heke C, Burfeind J, Hauschild K, et al. Ht-PEM fuel cell system with integrated complex metal hydride storage tank. Fuel Cells 2011;11:911–20.
[11] Li L, Xu C, Chen C, Wang Y, Jiao L, Yuan H. Sodium alanate system for efficient hydrogen storage. Int J Hydrogen Energy 2013;38:8798–812.
[12] Bogdanović B, Schwickardi M. Ti-doped alkali metal aluminium hydrides as potential novel reversible hydrogen storage materials. J Alloys Compd 1997;253–254:1–9.
[13] Bellosta von Colbe J, Lozano G, Metz O, Bucherl T, Bormann R, Klassen T, et al. Design, sorption behaviour and energy management in a sodium alanate-based lightweight hydrogen storage tank. Int J Hydrogen Energy 2015;40:2984–8.
[14] Zhang J, Xie Z, Zhang J, Tang Y, Song C, Navessin T, et al. High temperature PEM fuel cells. J Power Sources 2006;160:872–91.
[15] Kannan A, Kabza A, Scholta J. Long term testing of start-stop cycles on high temperature PEM fuel cell stack. J Power Sources 2015;277:312–6.
[16] Zhang G, Kandlikar SG. A critical review of cooling techniques in proton exchange membrane fuel cell stacks. Int J Hydrogen Energy 2012;37:2412–29.
[17] Na Ranong C, Höhne M, Franzen J, Hapke J, Fieg G, Dornheim M, et al. Concept, design and manufacture of a prototype hydrogen storage tank based on sodium alanate. Chem Eng Tech 2009;32:1154–63.
[18] Schmidt H, Buchner P, Datz A, Dennerlein K, Lang S, Waidhas M. Low-cost air-cooled PEFC stacks. J Power Sources 2002;105:243–9. 7th Ulmer Elektrochemische Tage.
[19] Zaluska A, Zaluski L, Ström-Olsen J. Sodium alanates for reversible hydrogen storage. J Alloys Compd 2000;298:125–34.
[20] Gross K, Thomas G, Jensen C. Catalyzed alanates for hydrogen storage. J Alloys Compd 2002;330332:683–90.
[21] Lozano G, Na Ranong C, Bellosta von Colbe J, Bormann R, Fieg G, Hapke J, et al. Empirical kinetic model of sodium alanate reacting system (I). Hydrogen absorption. Int J Hydrogen Energy 2010a;35:6763–72.
[22] Lozano G, Na Ranong C, Bellosta von Colbe J, Bormann R, Fieg G, Hapke J, et al. Empirical kinetic model of sodium alanate reacting system (II). Hydrogen desorption. Int J Hydrogen Energy 2010b;35:7539–46.
[23] Dedrick D, Kanouff M, Replogle B, Gross K. Thermal properties characterization of sodium alanates. J Alloys Compd 2005;389:299–305.
[24] Sandrock G, Gross K, Thomas G, Jensen C, Meeker D, Takara S. Engineering considerations in the use of catalyzed sodium alanates for hydrogen storage. J Alloys Compd 2002;330332:696–701. Proceedings of the International Symposium on Metal-Hydrogen Systems, Fundamentals and Applications (MH2000).
[25] Kandlikar SG, Lu Z. Fundamental research needs in combined water and thermal management within a proton exchange membrane fuel cell stack under normal and cold-start conditions. J Fuel Cell Sci Tech 2009;6:044001.
[26] Bird RB, Stewart WE, Lightfoot EN. Transport phenomena. Revised 2nd ed. John Wiley & Sons, Inc.; 2006.
[27] Lozano GA, Eigen N, Keller C, Dornheim M, Bormann R. Effects of heat transfer on the sorption kinetics of complex hydride reacting systems. Int J Hydrogen Energy 2009;34:1896–903.